



## Full length article

## Modelling and neutron diffraction characterization of the interfacial bonding of spray formed dissimilar steels

T.L. Lee <sup>a, b</sup>, J. Mi <sup>b, \*</sup>, S. Ren <sup>c</sup>, S. Zhao <sup>c</sup>, J. Fan <sup>c</sup>, S. Kabra <sup>a</sup>, S. Zhang <sup>a, d</sup>, P.S. Grant <sup>e</sup><sup>a</sup> ISIS Neutron Source, STFC Rutherford Appleton Laboratory, Harwell Campus, Didcot, OX11 0QX, UK<sup>b</sup> School of Engineering and Computer Science, University of Hull, Cottingham Road, Hull, HU6 7RX, UK<sup>c</sup> The Advanced Institute, Baosteel Co. Ltd., Shanghai, PR China<sup>d</sup> Centre of Excellence for Advanced Materials, Songshan Lake, Dongguan, Guangdong, 523808, PR China<sup>e</sup> Department of Materials, University of Oxford, Parks Road, Oxford, OX1 3PH, UK

## ARTICLE INFO

## Article history:

Received 25 December 2017

Received in revised form

3 May 2018

Accepted 23 May 2018

Available online 26 May 2018

## Keywords:

Finite element modelling

Neutron diffraction

Spray forming

Residual stresses

Dissimilar steels

## ABSTRACT

The spray forming of thick, dissimilar steel clad tubes with the objective of achieving a high integrity metallurgical bond across the cladding-substrate interface able to withstand residual stresses and subsequent thermo-mechanical processing was investigated by large scale experiments, modelling and extensive microstructural characterization including microscopy, X-ray tomography, neutron scattering and mechanical testing. The simulated residual stress distributions across the cladding-substrate interface, accounting for any as-sprayed porosity and the distribution of martensitic and retained austenite phases, were compared with neutron diffraction measurements and differences used to infer the load transfer behaviour and thus the mechanical integrity of the interface. The mechanical properties of the interfaces were then also measured directly by shear testing. The link between substrate pre-heating, the spray forming temperature, and the resulting preform temperature, porosity, phase fractions, residual stress, strength and integrity of the interface were established and quantified explicitly.

© 2018 Acta Materialia Inc. Published by Elsevier Ltd. This is an open access article under the CC BY license (<http://creativecommons.org/licenses/by/4.0/>).

## 1. Introduction

Spray forming involves the successive deposition of layers of an atomized alloy spray to build up a large bulk billet or near net shape component [1,2] and can also be used as a high deposition rate (20–40 kg min<sup>-1</sup> [3,4]) thick coating or cladding process, producing components comprising dissimilar alloys that provide functional and/or mechanical properties unavailable from a single alloy. For example, high wear resistance tool steels have previously been spray formed onto a high strength but lower cost commodity steel inner core for possible use as rolls used in metallic strip processing, realizing improved roll lives (>2 times [5]) compared with conventionally cast rolls due to refined carbide sizes, and a higher cost efficiency than monolithic rolls [6]. Although significant progress has been made on the spray forming aspects of clad products e.g. microstructural control, increasing process yield, ensuring low porosity, etc., there has been much more limited progress on understanding qualitatively how to promote interfacial

bonding between the substrate and the spray formed cladding. This bonding is critical because insufficient interfacial strength and toughness will typically lead to interfacial failure during downstream thermo-mechanical processing (TMP). TMP is usually required to eliminate a small fraction of residual as-spray formed porosity in the clad layer (typically <0.5%) and to increase further the integrity of the cladding-substrate interface [6].

The average spray temperature, and in particular, the substrate surface temperature during deposition, are known to be critical in promoting interfacial strength [6,7] and in avoiding excessive interfacial porosity [8,9] but there have been very few investigations to understand how these thermal aspects link explicitly to (i) the evolution of the stresses and strains in the substrate and the cladding that drive interfacial debonding, and (ii) the final integrity of the interfacial bond in a quantitative manner [10–14]. These residual strains can be sufficient to debond fully the interface during manufacture or immediately afterwards, and/or cause macroscopic distortions and cracking [15].

This paper presents an integrated experimental, modelling, microstructural and residual stress study of the spray forming of high speed steels onto mild steel tubes with a particular emphasis on understanding the relationship between the average droplet

\* Corresponding author.

E-mail address: [J.Mi@hull.ac.uk](mailto:J.Mi@hull.ac.uk) (J. Mi).

depositing temperature, substrate pre-heat temperature, phase fraction evolution, residual stresses, and bond strength across the interface. A coupled shape evolution, heat flow and thermal residual stress finite element (FE) model is developed and used to simulate the effects of substrate pre-heating on the residual stresses developed across the cladding-substrate interface. Residual stress predictions are then validated by comparison with a series of experiments including post spray forming measurements of residual stress obtained by neutron diffraction (ND) from sectioned circular rings taken from the spray formed clad tubes. Neutrons can penetrate up to a few centimeters into most metallic materials and thus, measurements are not confined to the surface region where stress relaxation often takes place [16]. For example, Lee et al. [14] used ND and X-ray micro-tomography ( $\mu$ CT) to characterize the 3D microstructures of a spray formed high speed steel, and correlated the microstructures and phase fractions with the residual stresses as a function of the deposition temperature. A similar ND approach was used by Kupperman et al. [17] to characterize the residual stress during the fabrication of high temperature ceramic superconducting composites bonded to a silver substrate. Finally, the shear strength of the interface under various conditions is investigated directly by mechanical testing.

The key features are: (1) the use of an internal substrate pre-heating technique that is shown to be critical to obtaining good interfacial bonding; (2) the incorporation of the local, evolving steel phase fractions and local porosity in the thermal residual stress model; (3) the use of X-ray micro-tomography to measure local porosity fractions and ND to measure local steel phase fractions and thermal stresses; and (4) the fusing of thermal, microstructural, diffusion, residual stress and interfacial mechanical property data to provide a comprehensive description of the factors governing the manufacture of high quality clad products by spray forming.

Although the model and experimental methods used are in the context of spray forming, they can be applied, in general, to any droplet spray deposition processes, especially where interfacial bonding of dissimilar materials exists, such as widely encountered in plasma spraying, cold spray, flame spraying, etc. There are also strong process physics similarities with additive manufacture processes where selective layer-by-layer melting and fusing of materials occur in the build process, and where significant residual stresses are also frequently problematical.

## 2. Experiments

### 2.1. Spray forming of dissimilar steel clad tube preforms

Approximately 40 kg of vacuum induction melted ASP30 (Fe-1.28C-4.2Cr-5Mo-6.4W-3.1V-8.5Co-0.5Mn-0.5Si wt.%) and M2 (Fe-0.9C-4.1Cr-5Mo-6.4W-1.9V-0.25Mn-0.35Si wt.%) high speed steels (HSS) were spray formed into claddings of >30 mm thick, reflecting the shape and size of small rolls used for strip processing, on thin (1.5–3 mm) mild steel tubes of 99–144 mm (inner) diameter. M2 steel was used initially to explore optimum spray parameters due to its lower cost than ASP30 that was used subsequently. Any differences in the thermophysical properties of the two steels were assumed negligible given their largely similar alloy composition and the significant variations in the more influential process parameters that were the principal focus of the investigation.

Fig. 1a shows schematically the droplet spray cone created by the two-stage free-fall atomizer with  $N_2$  as the atomization gas used in spray forming experiments [3]. The alloy droplet spray was mechanically scanned up to  $\pm 2.5^\circ$  using a sinusoidal scan pattern with a fixed frequency of 16.6 Hz. The droplets were sprayed and deposited onto rotating and retracting mild steel (Fe-0.25C-1.03Mn-0.2Cu-0.28Si wt.%) tube substrates to form dissimilar steel

tubes. The mild steel substrates were pre-heated using an induction heater (Ambrell Ltd) with induction coils inside the thin-wall tube substrate, as shown in Fig. 1a. The coil was fixed and the substrate rotated concentrically around the coil. The center of the spray cone was set at the midpoint of the induction heater coil length where the highest pre-heating substrate surface temperature was achieved as shown in Fig. 1b and c. The substrate surface temperature was measured using an embedded thermocouple (TC) and a two-color pyrometer (Land Instruments International Ltd). The mild steel substrate surface was grit blasted and degreased before spray forming. Eleven spray forming experiments were performed but only the four most interesting exploring the effects of pre-heating are presented in detail here. The substrate pre-heat and alloy droplet spray temperature was controlled by the induction heater input voltage and gas-to-melt flow ratio respectively. The key spray forming parameters are given in Table 1.

Supplementary video related to this article can be found at <https://doi.org/10.1016/j.actamat.2018.05.055>.

A steel plate was used to cover the entire substrate to shield the heated substrate from cooling due to the cold  $N_2$  gas flow before the melt was poured into the atomizer and spray forming started. Without such shielding, it was impossible to achieve sufficiently high and consistent surface temperature for the first few seconds of deposition when it is crucial to achieve bonding between the substrate and the first deposited material. The shield was also useful in catching the first few seconds of atomized spray, which is typically relatively unstable. After that, a steady flow of liquid steel through the atomizer was established. When the spinning substrate reached the defined temperature and after a few seconds of deposition on the shield, the shield was laterally withdrawn at high speed using a powerful pneumatic ram. In this way, steady spray deposition onto a pre-heated substrate with defined temperature was achieved for the majority of the spray forming process. Of course, towards the end of the process, the melt flow rate reduced as the tundish was exhausted and the associated transient effects on the shape, thermal history and thermal stresses development were also taken into account in the model, as described below.

### 2.2. Shape, thermal history and thermal stress evolution model

The model formulation for the shape evolution and thermal history of the cladding as it forms during spray forming has similarities with our previous work and details are thus given in the Supplementary Materials. The critical thermal residual stress development aspects have not been explored before, and were formulated as follows.

#### 2.2.1. Thermal residual stress model development

Linking with the thermal and shape models described in the Supplementary Materials, the thermal residual stresses in the clad tubes were simulated using the Thermal Stress sub-module in COMSOL Multiphysics<sup>®</sup> using isotropic and linear elastic material assumptions.

Thermal residual stresses in sprayed dissimilar alloy components are developed when a mismatch in strain arises during cooling due to the differences in temperature distribution and coefficient of thermal expansion (CTE,  $\alpha$ ) between the constituent materials [18]. In the case of spray formed high speed steel, the local CTE is dependent on the relative fractions of the different steel phases that may form, because the phases have markedly different CTEs. Neutron diffraction showed that the two phases always present in resolvable fractions in the cladding were martensite ( $\alpha'$ -Fe) and retained austenite ( $\gamma$ -Fe), and the effective, local CTE ( $\alpha_{\alpha'+\gamma}$ ) was thus calculated simply using a rule-of-mixtures:

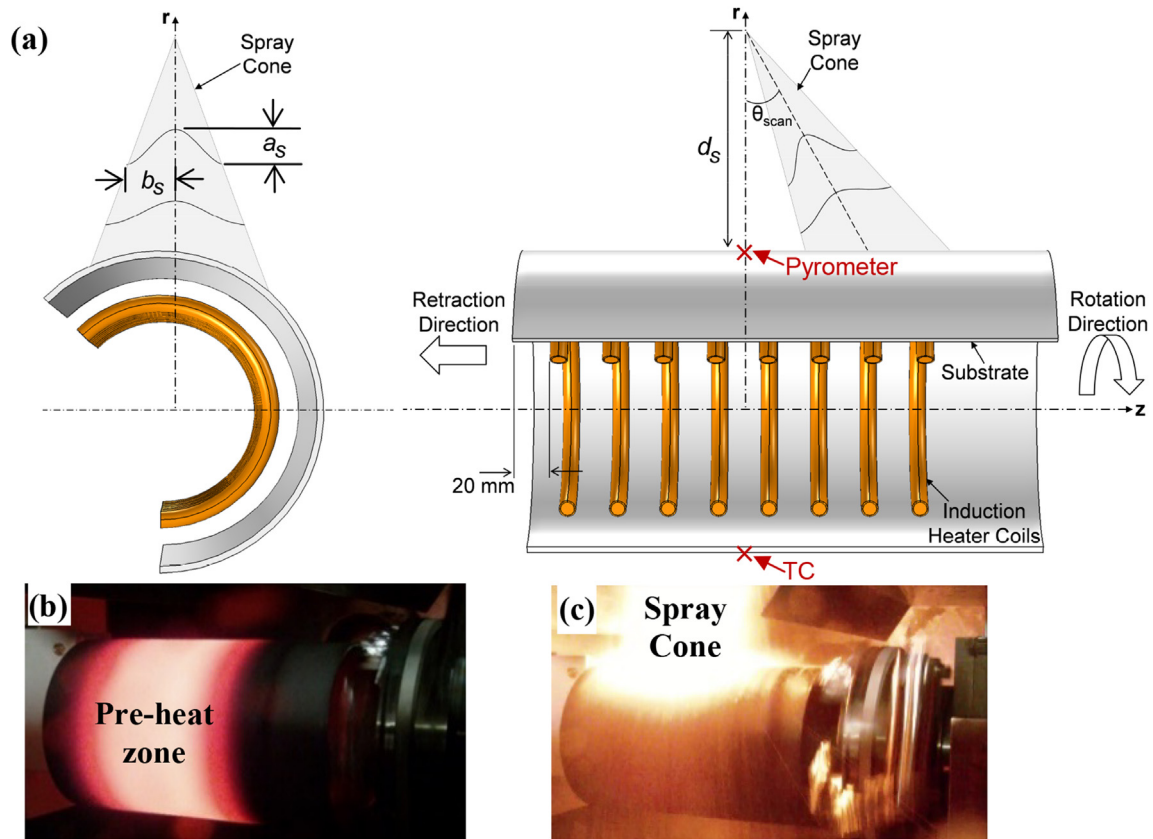


**Fig. 1.** (a) Cross-sectional schematic views of the spray forming arrangement, showing the induction heater coils inside the tube substrate and the initial deposition position at the midpoint of the induction heater coil length (the maximum substrate surface temperature). The pyrometer and thermocouple (TC) measurement positions are marked with the red “x”. (b) A photo of the pre-heated substrate immediately before spraying commenced showing the high temperature but relatively narrow pre-heat zone and (c) the atomized metallic droplets in the spray cone depositing onto the pre-heated zone. See simulation [Video 1](#). (For interpretation of the references to color in this figure legend, the reader is referred to the Web version of this article.)

**Table 1**  
The spray forming parameters.

	Non pre-heated		Pre-heated	
Clad tube experiment designation	NP1	NP2	P1	P2
Cladding	M2	M2	ASP30	ASP30
Substrate inner diameter (mm)	104	99	144	144
Substrate thickness (mm)	3.0	1.5	3.0	3.0
Substrate rotation speed (rps)	2.0	2.2	1.7	1.7
Substrate retraction speed (mm s <sup>-1</sup> )	2.40	1.60	0.57	0.83
Induction heater input voltage (V)	N/A	N/A	400	450
Spray distance, $d_s$ (mm)	500	550	600	600
Atomizer scan angle, $\theta_{scan}$ (°)	0.0	±2.0	±2.5	±2.5
Average melt flow rate (kg s <sup>-1</sup> )	0.65	0.32	0.29	0.32
Average gas flow rate (kg s <sup>-1</sup> )	0.34	0.18	0.18	0.18
Gas-to-melt flow ratio (GMR)	0.52	0.56	0.61	0.56
Mean sticking efficiency (SE)	0.65	0.71	0.73	0.68

$$\alpha_{\alpha'+\gamma} = f_{\alpha'}\alpha_{\alpha'} + f_{\gamma}\alpha_{\gamma} \quad (1)$$

where  $\alpha_{\alpha'} = 11.6 \mu\text{K}^{-1}$  [19] and  $\alpha_{\gamma} = 18.7 \mu\text{K}^{-1}$  [20] are the mean CTE of  $\alpha'$ -Fe and  $\gamma$ -Fe up to 922 K respectively, and the corresponding phase weight fractions (PWFs)  $f_{\alpha'}$  and  $f_{\gamma}$  were determined by fitting to the neutron diffraction data, as described later. The mild steel substrate was assumed to have a mean CTE of  $14.4 \mu\text{K}^{-1}$  over the temperature range [21]. The calculated transient temperature distributions are used to calculate the thermal strain  $\epsilon_{th}$  in the cladding using:

$$\epsilon_{th} = \alpha (T - T_{sf}) \quad (2)$$

where  $T$  is temperature and  $T_{sf} = 1158 \text{ K}$  is the assumed stress-free temperature above which the steel dissipated any strains via creep or other high temperature plastic processes [22]. The thermal residual stress  $\sigma$  is then calculated using:

$$\sigma = C_{el} : (\epsilon - \epsilon_{th}) \quad (3)$$

where  $C_{el}$  is the fourth order elasticity tensor and  $\epsilon$  is the total strain

tensor. In addition to the boundary conditions specified for the thermal model, rigid body movement in the thermal residual stress model was prevented by constraining the clad tube axial direction (z-axis) displacement of one of the vertices along the substrate inner surface to zero. The thermophysical properties of the steel claddings and mild steel substrate are given in Table S2 in the Supplementary Materials.

### 2.3. Microstructural characterization of the porosity and interface

#### 2.3.1. X-ray $\mu$ CT characterization of porosity distribution

Since the as-sprayed cladding, like all spray formed materials, is always porous to some extent, the effect of porosity on the mechanical properties of the cladding i.e. Young's modulus and Poisson's ratio, was also taken into account. The Young's modulus of the porous cladding  $E^*$  was calculated using the model developed for porous sintered steels [23,24]:

$$E^* = E \left[ \frac{(1-P)^2}{1 + (2-3\nu)P} \right] \quad (4)$$

where  $E$  is Young's modulus,  $\nu$  is Poisson's ratio, and  $P$  is the porosity fraction in the steel. The Poisson's ratio of the porous cladding  $\nu^*$  was determined using:

$$\nu^* = \nu + \frac{P}{P_\infty}(\nu_\infty - \nu) \quad (5)$$

where  $P_\infty = 0.472$  and  $\nu_\infty = 0.14$  for porous steels [25].

Because no robust model for the prediction of residual spray formed porosity fraction exists, porosity was introduced into the FE model on the basis of post-deposition microstructural analysis correlated to the instantaneous deposition temperature at that point. The post-deposition through-thickness porosity distributions were measured by X-ray micro-tomography ( $\mu$ CT). Cross-sectional strip samples near to the thickest region of the as-sprayed claddings were cut using electrical discharge machining (EDM) and then machined into 1 mm diameter rods for porosity distribution characterization along the cladding thickness using a lab-based  $\mu$ CT scanner (HMX 160; X-Tek Systems) with a spatial resolution of  $\sim 3 \mu\text{m}$  per pixel. The 3-D tomography data-sets were segmented using Avizo<sup>®</sup> software and porosity was quantified within 1 mm segments through the cladding thickness, from the interfacial region, out to the cladding upper free surface.

In order to investigate microstructural features in the interface region in more detail, synchrotron X-ray  $\mu$ CT characterizations were also performed at the TOMCAT beamline (Paul Scherrer Institute, Switzerland) with monochromatic X-rays (42 keV). Samples were cut from clad tube P2 and the X-ray beam transmitted through the sample was detected using a  $20 \mu\text{m}$  thick LAG:Ce scintillator and high resolution imaging detector (PCO.edge 5.5). The sample was rotated at steps of  $0.12^\circ$  over  $180^\circ$  and each scan comprised of 1501 projections with an exposure time of 1.9 s per projection and a spatial resolution of  $0.65 \mu\text{m}$  per pixel.

#### 2.3.2. Microstructure and elemental diffusion profiles measurement

To investigate the cladding microstructure, the interfacial bonding and elemental diffusion profiles across the cladding and substrate, cross-sectional samples near to the thickest region of the clad tubes were cut, ground, polished and then analyzed using scanning electron microscopy (SEM, Cambridge Instruments Stereoscan S-360) and energy dispersive X-ray spectroscopy (EDS) in the SEM (JEOL JSM-6500 F) at 20 kV accelerating voltage. Interfacial diffusion profiles were investigated and related to the extent of any interfacial metallurgical bonding and mechanical interaction

between cladding and substrate.

### 2.4. Neutron diffraction characterization of phase and residual stress distribution

The time-of-flight (TOF) neutron diffractometer ENGIN-X housed at ISIS Neutron Source, UK [16] was used to characterize and quantify non-destructively the phase fraction and residual stress profiles in the interface region of the clad tubes. Ring-shaped cross-sectional samples (10 mm width) near to the thickest region of the clad tubes were cut via EDM for the neutron diffraction (ND) characterization.

#### 2.4.1. Residual stress characterization

Fig. 2a shows the ND experiment set-up at ENGIN-X to map residual stresses in the sectioned spray formed clad tubes. Seven measurement points (marked as red points in Fig. 2b) were taken through the cladding thickness. A gauge volume (GV) of  $2 \times 2 \times 2 \text{ mm}^3$  was used to optimize between spatial resolution (especially near to the interface region) and neutron counting times. Only one measurement point was possible in the relatively thin mild steel substrate (3 mm) because it was necessary that the GV was completely filled with only the steel substrate to avoid pseudo-strains [26]. Due to symmetry, the principal residual stresses in the sample can be derived by measuring the three principal strains [27]: hoop ( $\epsilon_\theta$ ), axial ( $\epsilon_z$ ) and radial ( $\epsilon_r$ ) strains. Two of the principal strain components can be measured simultaneously from each measurement point during a scan. The remaining strain component was measured from the same measurement points but with the sample rotated at  $90^\circ$  around the axial axis (see Fig. 2a). Assumed stress-free samples with lattice spacing ( $d_0$ ) were obtained as  $5 \times 5 \text{ mm}^2$  cross-sectional coupons (Fig. 2c) cut from each clad tubes using EDM and investigated by ND to ensure a consistent microstructure in both the reference and the sample. The reference coupon sections were assumed stress-free as they were unconstrained by any macroscopic stress field, whereas all the samples of the clad tubes comprised whole circular clad ring sections with no relief of macroscopic residual stresses in the hoop direction. The Bragg peaks in the neutron diffractograms were fitted using the whole-pattern Rietveld refinement method [28] with GSAS [29] to derive the local lattice spacing ( $d$ ) and phase weight fractions (PWF). Detailed information regarding the PWF analysis using Rietveld refinement is described in Ref. [30].

The residual strain in the ring-shaped cross-sections was calculated using  $\epsilon = (d - d_0)/d_0$ . The residual stress  $\sigma$  was calculated for each phase from the residual strains using Hooke's law:

$$\sigma_i = \frac{E}{1+\nu} \left[ \epsilon_i + \frac{\nu}{1-2\nu} (\epsilon_r + \epsilon_\theta + \epsilon_z) \right] \quad (6)$$

where the subscript  $i$  denotes the respective principal stress components. The residual macro-stress was determined using a rule-of-mixtures [14]:

$$\sigma_{\alpha'+\gamma} = f_{\alpha'} \sigma_{\alpha'} + f_{\gamma} \sigma_{\gamma} \quad (7)$$

with the phase-specific stresses ( $\sigma_{\alpha'}$  and  $\sigma_{\gamma}$ ) calculated using Eq. (6) with the Young's Modulus  $E = 200 \text{ GPa}$  for  $\alpha'$ -Fe [19] and  $E = 193 \text{ GPa}$  for  $\gamma$ -Fe [20].

#### 2.4.2. Phase fraction characterization

In atomized high speed steels, the droplets experience high cooling rates ( $\sim 10^2$ – $10^4 \text{ K s}^{-1}$  [2]) that give rise to the formation  $\alpha'$ -Fe and retained  $\gamma$ -Fe. However, in spray forming, these droplets are



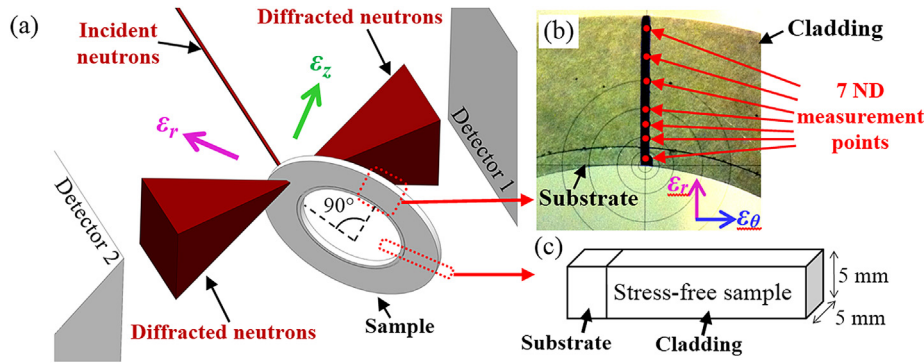


**Fig. 2.** (a) A 3D schematic of the ND experiment set-up showing the two measured strain components from a scan point and the sample rotation angle used to measure the third strain component. (b) A photo of the cross-sectional sample cut from clad tube NP1 showing the 7 measurement points (marked as red points) taken along the preform thickness. (c) A schematic of the stress-free cross-sectional coupon. (For interpretation of the references to color in this figure legend, the reader is referred to the Web version of this article.)

reheated rapidly as they are incorporated in the growing cladding, which is usually mushy. As the cladding thickens, the final reheat temperature and time spent at high temperature increases, giving rise to higher fraction of retained austenite ( $f_\gamma$ ) in the cladding once it cools slowly at the end of deposition [31]. These transient conditions affect the resulting martensite and retained austenite fractions at room temperature and must be accommodated in the thermal stress model since as already explained they have a direct effect in controlling the local thermophysical properties at any instant, such as CTE. Using the measured retained austenite phase weight fraction  $f_\gamma$  obtained by ND, the local martensite start temperature ( $M_s$ ) was estimated according to [32]:

$$f_\gamma = \exp[-k(M_s - T)] \quad (8)$$

where the constant  $k = 0.0128$  for a similar tool steel [33], and  $f_{\alpha'} = 1 - f_\gamma$ . The austenite-to-martensite transformation is also governed by the cooling rate and thus  $k$  in Eq. (8) changes according to the cooling rate. Because the cooling rate after the spray ended and atomizer gas flow stopped is expected to be relatively uniform throughout the metallic cladding during slow cooling, a fixed  $k$  value from a similar tool steel under similar cooling rates [33] was used.

By fitting a best-fit line through the data of experimentally derived local  $M_s$  from Eq. (8) as a function of the simulated cladding temperature immediately at the instant when deposition ended and cooling started, a best-fit correlation was established to predict the final volume fraction of retained  $\gamma$ -Fe and  $\alpha'$ -Fe anywhere in the cladding, and thus, the local CTE distribution using Eq. (1). At temperatures above the local  $M_s$ , the cladding was assumed to consist of only retained austenite ( $f_\gamma = 1$ ) with a CTE of  $\gamma$ -Fe =  $18.7 \mu\text{K}^{-1}$ .

### 2.5. Interfacial bond strength measurement

The interfacial bond strength of clad tubes was determined by shear testing according to the EN 15340 standard [34]. The in-house machined shear test rig was mounted onto an Instron 50 kN load frame. Specimens used in the shear test were cut via waterjet cutting from the clad tube cross-sections (Fig. 3) where there was relatively good bonding and the surfaces of the specimens were ground (1200 grit) to a final dimension of  $\sim 30 \times 10 \times 5$  mm (30 mm along the cladding thickness direction). The edge of the shear plate was positioned at  $\sim 50 \mu\text{m}$  from the cladding-substrate interface (shear distance) as shown in Fig. 3.

A shear load was applied parallel to the cladding-substrate interface via a carbide shear plate (Sandvik SP EW 120408) while

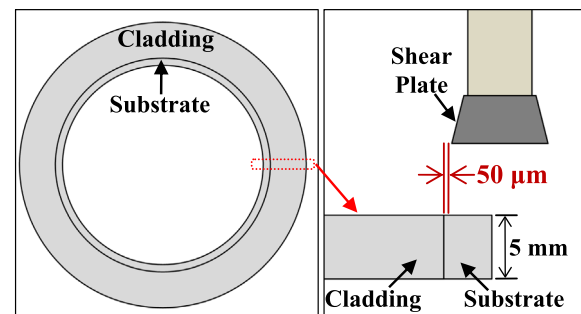


**Fig. 3.** A schematic showing the position of the shear test specimen that was cut from the cross-section of the clad tube (indicated by red dotted bounding box) and the orientation of the shear test specimen to the shear plate tool. (For interpretation of the references to color in this figure legend, the reader is referred to the Web version of this article.)

the cladding section was held securely. The direction of the applied shear load was therefore along the hoop direction of the clad tube and was the most relevant direction to assess the integrity of the cladding-substrate interface. The shear load was applied to the substrate rather than the spray formed cladding because the substrate was relatively thin (3 mm) and more awkward to hold securely. The load frame crosshead speed was  $0.05 \text{ mm s}^{-1}$  and the applied load was increased steadily from 50 N until delamination or other failure occurred. The bond strength was calculated using the maximum force at which failure occurred from at least five specimens for each clad tube.

## 3. Results

### 3.1. Interface microstructure

Cross-sectional microstructural examination of the clad tubes revealed that NP1 and NP2 (e.g. in Fig. 4a, without pre-heating) showed macroscopic cracks and delamination whereas P1 (with pre-heating) was completely detached from the substrate. P2 (with pre-heating) in Fig. 4b showed no visible macroscopic cracking or delamination along the interface. At higher magnification, only the P2 interface showed no evidence of significant cracking or porosity (see Fig. 4b). Fig. 4c shows part of a synchrotron X-ray  $\mu\text{CT}$  tomogram acquired from the interface region of clad tube P2. The boundary between the cladding and substrate could be delineated in the tomogram due to the difference in Fe concentration between the steels that produced a resolvable change in the X-ray absorption

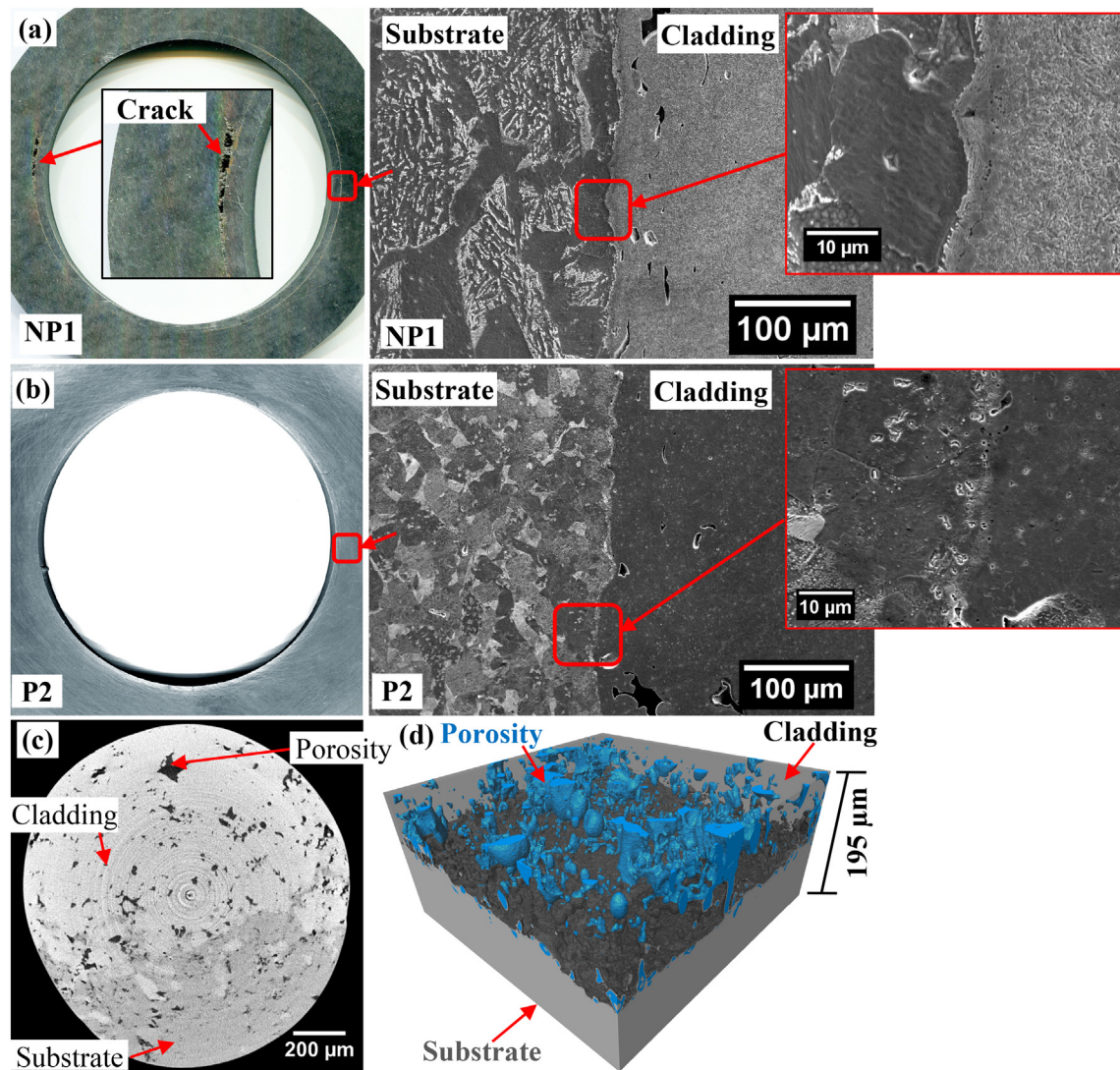


**Fig. 4.** (a–b) Cross-sectional macro-structure and the corresponding high magnification scanning electron micrographs (secondary electron image) of the cladding-substrate interface region of spray formed clad tubes NP1 and P2 respectively. (c) A synchrotron X-ray  $\mu$ CT tomogram acquired from the interface region of clad tube P2, and (d) the corresponding 3-D rendering of the porosity (in blue) segmented from the tomograms. (For interpretation of the references to color in this figure legend, the reader is referred to the Web version of this article.)

contrast (higher Fe content = darker). The morphology of the porosity (up to  $\sim 100 \mu\text{m}$  in diameter) is shown in the 3-D rendering of porosity in Fig. 4d, segmented from the tomograms acquired from the near-interface region.

The interface region of clad tubes NP1 and P2, where there was relatively good bonding, was investigated using EDS and the elemental maps in Fig. 5a and b show across-interface diffusion of W, Mo and Fe from the cladding into the substrate, with an interdiffusion zone of  $\sim 5 \mu\text{m}$  (indicated by the white dotted lines). The interdiffusion is shown in more detail in the EDS line-scans taken across the interface in Fig. 5c and d. Distinct peaks in the W and Mo line-scan profiles associated with the carbides in the cladding of P2 are also resolved in Fig. 5d.

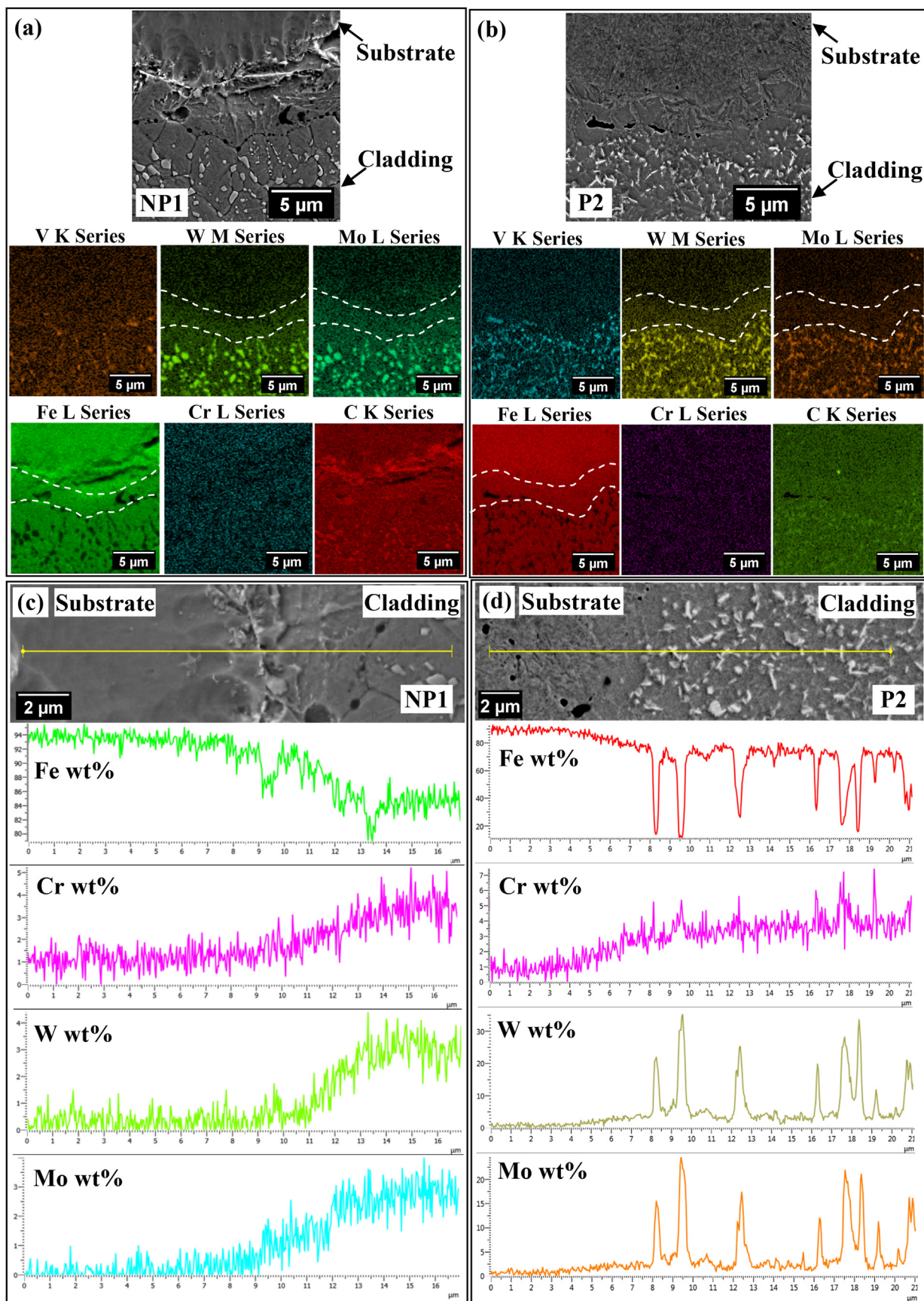
In order to confirm that the interdiffusion zone in the elemental mapping was not due to an EDS interaction volume effect, the approximate size of the X-ray excitation region from the interaction volume was calculated using the Andersen-Hasler X-ray excitation range equation [35]. At 20 kV accelerating voltage, the X-ray excitation region size was estimated at  $\sim 1.1 \mu\text{m}$  for a Fe matrix. Therefore, compared with the  $\sim 5 \mu\text{m}$  thick interdiffusion zone, the EDS

spatial resolution was sufficient to provide a reasonable estimate of the thickness of the interdiffusion zone, and confirmed there was enduring, intimate substrate-cladding contact.

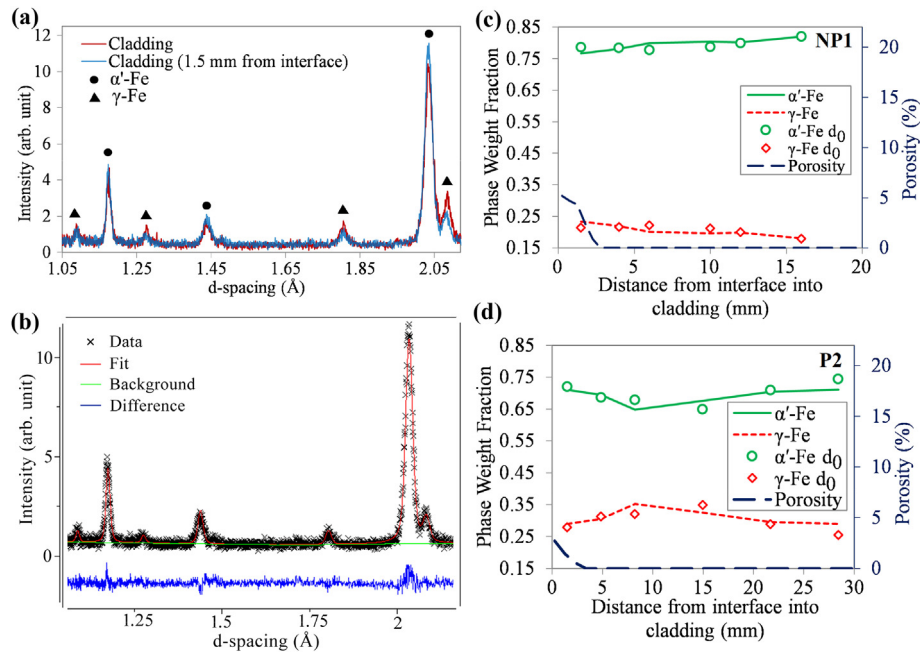
### 3.2. Thermal history and microstructure distribution

Fig. 6a shows two typical neutron diffractograms from the spray formed cladding in which the dominant phases were martensite ( $\alpha'$ -Fe) and retained austenite ( $\gamma$ -Fe), within 1.5 mm of the interface, and within the bulk of the cladding. Fig. 6b shows a corresponding example of the fitted diffractogram (Rietveld refinement) used to derive the phase lattice spacing and to estimate the phase weight fractions (PWF). The lower blue line is the difference between experiment data and fit, and suggested good agreement of the best-fit trace to the data. PWF distributions from the cladding and assumed stress-free reference samples cut from clad tubes NP1 and P2 are shown in Fig. 6c and d respectively. There were similar martensite and retained austenite phase fractions through the cladding thickness, up to 30 mm from the interface. Fig. 6c and d also show plots of the local porosity obtained from the





**Fig. 5.** EDS elemental distribution map of the interface region of clad tube (a) NP1 and (b) P2. The interfacial diffusion region is indicated by white dotted lines. Corresponding EDS line-scan taken along the marked yellow line across the interface region of clad tube (c) NP1 and (d) P2, for Fe, Cr, W and Mo. (For interpretation of the references to color in this figure legend, the reader is referred to the Web version of this article.)



**Fig. 6.** (a) Neutron diffractograms taken from both relatively dense and porous regions (1.5 mm from the interface) of the as-sprayed cladding and (b) an example of a Rietveld best-fit diffractogram. Phase weight fractions of  $\alpha'$ -Fe and  $\gamma$ -Fe through the cladding thickness for both an integral ring section and for the assumed stress-free coupon, for clad tube (c) NP1 and (d) P2, with the through thickness porosity distributions superimposed.

tomograms, showing that beyond the porous interfacial region and top free surface, most of the cladding had a density  $>99.5\%$ .

Fig. S4 in the Supplementary Materials shows examples of the good agreement between the simulated and experimental cladding shape for all four experiments. The cladding thickness along the tube substrate length varied due to the relatively low substrate retraction speed used and the relatively high metal flow rate so that an extended length of cladding was not produced, but rather a shorter thicker region more typical of small rolls. All microstructural, interfacial bond and residual stress assessments were performed on material taken from the thickest region of the cladding. Fig. S5 shows similar good agreement between simulated and measured temperatures, and Fig. S6 shows how different assumed values of the heat transfer coefficients were explored to arrive at best-estimate heat transfer coefficient values that gave consistent agreement with experiments. Fig. S7 shows the through-thickness simulated cladding temperature for NP1 and P2 immediately after deposition, the estimated local PWF for  $\gamma$ -Fe, and the local  $M_s$  best-fitted to Eq. (8) based on the measured PWF. Fig. 7a shows the simulated temperature distributions in the pre-heated clad tube P2 at different spraying times. As expected, the mushy zone of the growing cladding was displaced axially as the substrate was slowly retracted axially to widen the region of clad material, leading to a non-symmetrical instantaneous temperature distribution. As expected, the  $\gamma$ -Fe fraction was higher in regions where the preform temperature was highest, such as in the middle regions of the cladding, while colder regions towards the substrate and free surface had slightly higher fractions of  $\alpha'$ -Fe. The parameters of the best-fit relationship between the local martensite start temperature  $M_s$  from Eq. (8) and simulated preform temperature immediately after spraying for clad tubes NP1 and P2 are shown in Table 2.

Using the correlations in Table 2, the simulated 2D, axisymmetric  $\alpha'$ -Fe distribution throughout the entire as-sprayed clad tube P2 at room temperature is shown in Fig. 7b, with a higher local fraction of  $\alpha'$ -Fe towards the edges of the cladding where the spray was colder and the deposition rate lowest. Using this data and Eq.

(1), Fig. 7c shows how the local CTE, which will directly affect residual strains, must therefore also vary locally, with the largest effective CTE in the hottest centre of the cladding, with the highest austenite fraction.

The porosity distributions through the clad region for the non pre-heated and pre-heated clad tubes are shown in Fig. 8a and b respectively. The corresponding simulated cladding top surface layer temperature ( $T_{\text{Layer}}$ ) at that point during manufacture are superimposed on Fig. 8a and b. All claddings showed a layer of porosity extending into the cladding from the interface. Pre-heating reduced the porosity fraction in this region by  $>50\%$ , and higher cladding layer temperatures during spraying reduced the porous layer thickness by up to  $\sim 2$  mm. Although the cladding alloy used in the non pre-heated and pre-heated clad tubes was different, any differences in the thermophysical properties between the two clad steels are judged to be of limited influence given the other more significant changes in the process parameters (Table 2). This assumption is at least partly supported by the similar porosity profiles with respect to local thermal conditions in the different steel claddings, as discussed below.

Beyond the thermal/microstructural transient zone close to the interface, porosity in all cases was  $<0.5\%$  where Fig. 8 shows there were also pseudo-steady state thermal condition, with an alloy liquid fraction  $f_l \geq 0.20$  during deposition, consistent with previous work on spray formed steel cladding [10]. In the initial transient zone, comparison of estimated liquid fractions and resulting porosity suggested that a minimum of  $f_l = 0.20$  was required to avoid porosity  $>1\%$ , and a maximum liquid fraction of up to  $f_l = 0.70$  might be acceptable, from a porosity point of view, although macroscopic surface perturbations might also then occur (see Fig. S4a in the Supplementary Materials). Therefore, there is a trade-off between low porosity and acceptable cladding surface quality/shape definition. In this study, this compromise was reached by increasing the spray distance to allow the spray to achieve a slightly lower liquid fraction and to reduce the deposition rate per unit area (as the spray cone of material diverged), and then



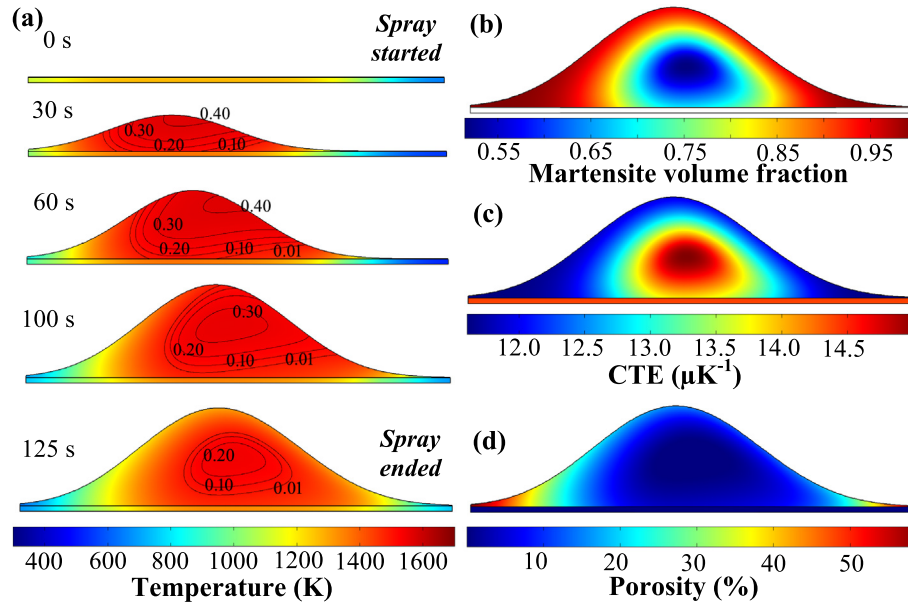


**Fig. 7.** (a) The simulated temperature distributions in the pre-heated clad tube P2 at different spraying times. (b) The overall 2D axisymmetric martensite volume fraction distribution in the as-sprayed cladding P2, (c) the effective CTE distribution as a result of the local fractions of martensite and austenite, and (d) the corresponding porosity distribution based on Eq. (9). See simulation [Video 1](#).

**Table 2**

Best-fit correlations between local martensite start temperature  $M_s$  and simulated cladding temperature  $T$  immediately after deposition for clad tubes NP1 and P2.

Clad tube	Cladding	Correlation
NP1	M2	$M_s = -0.643 \times T + 1413$
P2	ASP30	$M_s = -0.513 \times T + 1135$

to compensate for the associated lower enthalpy flux by pre-heating to minimize the “cold” transient region of relatively high porosity that would otherwise be promoted. However, the intended effect of pre-heating was not only to provide an extra degree of freedom in this macro-scale heat balance consideration, but also to promote micro-scale interfacial diffusion to improve the quality of the interface, and thus to affect the final room temperature distribution of through-thickness residual stresses. By combining the microstructural measurements and the simulations, larger fractions of porosity were suggested in the interface and surface regions of the cladding when  $T_{\text{Layer}}$  was lower than the alloy temperature at which  $f_L = 0.20$  ( $T_{f_L=0.20}$ ), and the porosity fraction

gradually increased as  $T_{\text{Layer}}$  decreased. The porosity fraction in the interface region was reduced by pre-heating the substrate because higher liquid fractions were sustained in this region otherwise colder region.

By fitting a best-fit line through the data of local porosity ( $P$ ) versus the simulated cladding layer temperature at which it was formed ( $T_{\text{Layer}}$ ) relative to the alloy temperature at which  $f_L = 0.20$  ( $T_{f_L=0.20}$ ) as shown in [Fig. S8](#) in the Supplementary Materials, a correlation was established of the form:

$$P = -0.065(T_{\text{Layer}} - T_{f_L=0.20}) \quad (9)$$

where  $P = 0$  at  $T_{\text{Layer}} > T_{f_L=0.20}$ . Using this correlation and the calculated temperature distribution, the porosity distribution anywhere within the cladding could then be approximated. Using this approach, [Fig. 7d](#) shows the simulated 2D axisymmetric porosity distribution throughout clad tube P2 with relatively high porosity formed at the extreme edges of the cladding where the spray was colder, and the deposition rate per unit area was the lowest, consistent with microstructural observations.

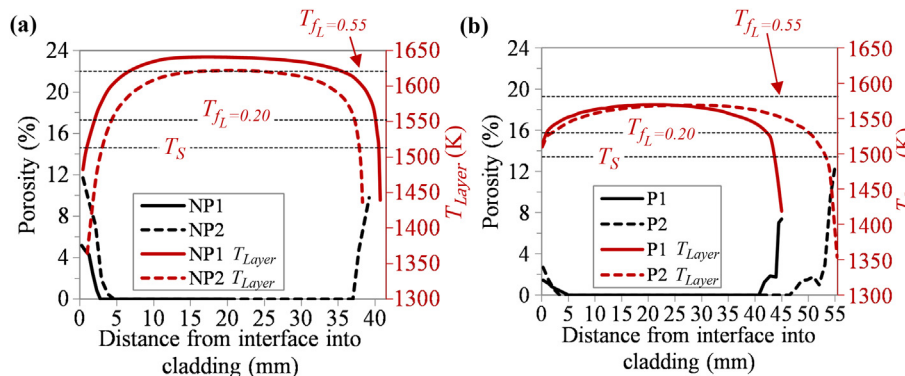


**Fig. 8.** The porosity distribution obtained by X-ray  $\mu\text{CT}$  through the as-sprayed (a) non pre-heated and (b) pre-heated clad tube thickness, together with the simulated cladding layer temperatures at that point during manufacture, and various alloy solid fractions.

### 3.3. Residual stress distribution

Fig. 9a and b show the FE simulated and ND measured residual hoop stress distributions across the cladding-substrate interface of clad tubes NP1 and P2 respectively. In general, the simulated residual stress distributions showed a tensile stress of ~310 MPa in the substrate while compressive stresses of up to ~30 MPa were present in the cladding, immediately adjacent to the interface. The steep change in stress across the cladding-substrate interface was due to the CTE discontinuity between the substrate and cladding, as shown by the plot of local CTE distributions based on ND measurements of local phase fractions superimposed in Fig. 9.

### 3.4. Interfacial shear strength

The interfacial shear strength of specimens cut from clad tubes NP1 and P2 are given in Table 3. Because the strength of the bond formed is not expected to exceed the strength of the substrate or the as-sprayed cladding material, the shear strength of the interface is presented as a simple ratio of the interfacial shear strength to the mild steel substrate shear strength (338 MPa). The interfacial shear strength of NP1 was consistently lower than that of P2, and showed a larger variation due to previously described local variability in the bond integrity along the interface. The interfacial shear strength of the pre-heated clad tube P2 was more consistent, with a mean shear strength of ~93% of the shear strength of the mild steel substrate.

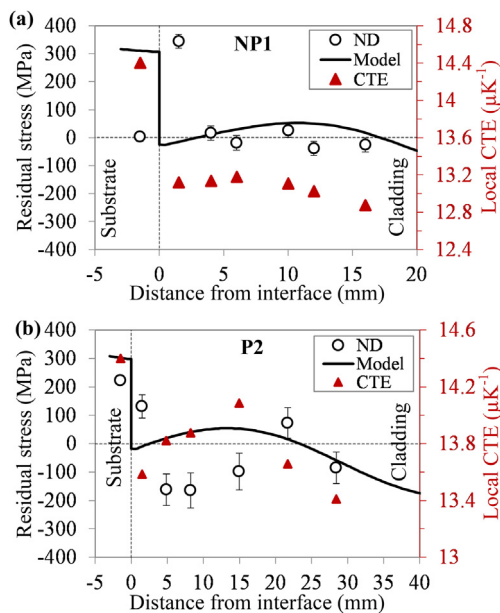


Fig. 9. The simulated and ND measured residual hoop stress distributions across the cladding-substrate interface of clad tubes (a) NP1 and (b) P2, with the local CTE derived from the ND measurements of local phase fractions and Eq. (1) superimposed.

## 4. Discussion

### 4.1. Interface mechanical integrity

The cladding-substrate interface was modelled as perfectly bonded i.e. no gaps/voids or relative movement between the cladding and substrate surfaces. The simulated, idealized thermal residual stress distribution therefore served as a benchmark against which the experimentally measured distribution could be compared to infer the mechanical integrity of the interfacial bonding. This approach is justified because significant residual stress in the relatively slow cooling cladding (after spraying ended) can only be developed when strong bonding at the interface constrains both the substrate and cladding. In contrast, in the absence of a strong interfacial bond that can inhibit contraction or transfer load, residual stress in the cladding will be small because the mild steel substrate has a higher CTE than the as-sprayed cladding, it will contract more than the cladding during cooling, and will thus result in little cladding-substrate thermo-mechanical interaction i.e. only if the interface is mechanically sound will the differential thermal expansion/contraction behaviour be coupled and significant stresses evolve. Therefore, differences or similarities in simulated (ideal) and measured (actual) stresses may be indicative of the mechanical integrity of bonding. Stresses in the axial direction could not be assessed in this study since they are significantly relaxed when the ring cross-section sample is sectioned from the clad tube.

The simulated and measured residual hoop stresses in the substrate are given in Table 3. The low residual stress (~3 MPa) measured in the substrate of clad tube NP1 is only ~1% of the simulated stress, which implies that the substrate was unconstrained during thermal excursions, and that there was poor/no interfacial bonding in the region of the preform where ND measurements were acquired. Although the microstructure in this region (see Fig. 5a and c) suggested that the substrate surface and spray temperatures exceeded the critical threshold temperature required that may lead to some interfacial diffusion and bonding [6,7], the macroscopic crack formed along the interface of NP1 (see Fig. 4a) prevented any significant interdiffusion zone and metallurgical interfacial bonding so that overall, the substrate and cladding were insufficiently integrated to generate significant CTE mismatch stresses. On the other hand, a tensile residual stress of ~222 MPa was measured in the substrate of the pre-heated clad tube P2, which was ~73% of the simulated stress, and by comparison with the previous case, suggested a relatively high mechanical integrity bond. Qualitatively, the findings are in agreement with the subsequent shear test results (see Table 3) that showed higher interfacial shear strengths when optimized pre-heating and spray temperatures were used for cladding P2.

The discrepancy between the simulated and ND measured residual stresses through the cladding thickness, even for clad tube P2 that had a relatively good interfacial bond, may be due to the inaccuracies in the assumed physical properties (i.e. Young's modulus and Poisson's ratio) of the steels. Nevertheless, the general trend of the measured stress distribution agreed reasonably well with the modelled stress distribution except for the measured

Table 3

The substrate residual hoop stresses for clad tubes NP1 and P2, and the corresponding interfacial shear strengths.

Clad tube	Substrate residual hoop stress			Shear strength		
	ND (MPa)	Model (MPa)	ND/Model	Bond (MPa)	Substrate (MPa)	Bond/Substrate
NP1	2.6	311.61	1%	192 ± 33	337.5	57%
P2	222.3	302.89	73%	313 ± 11	337.5	93%

stresses at  $\sim 1.5$  mm from the interface where a relatively high tensile stress of up to  $\sim 350$  MPa was developed. This was very likely due to porosity-induced errors in the ND measurement in regions of relatively high porosity close to the interface (see Fig. 8a and b). Because the as-sprayed cladding is porous in the interface and surface region, the neutron scattering material density differences in the GV may give rise to errors (pseudo-strains) in residual strains in these regions [14]. Although pseudo-strains caused by scattering material density differences in the GV can be computed and corrected [26], it was not feasible to perform this correction because the GV ( $= 8 \text{ mm}^3$ ) was not sufficiently larger than the length scale of the porosity in the cladding (typically  $10^{-3}$ – $10^{-2} \text{ mm}^3$ , see Fig. 4c and d) and thus, localized variations in the residual strain direction caused by the porosity free surfaces could not be assumed to be averaged out over the length scale over which residual strains were measured. Nevertheless, only one of the seven ND measurement points acquired from each cross-sectional sample was within the significantly porous layer (up to 3 mm thick from the interface) and the overall trend of residual stress distribution in the claddings was not affected significantly.

#### 4.2. Effect of substrate pre-heat and spray temperature on residual stress and interfacial bonding

Fig. 10a and b show the hoop stress as a function of post-spray time (time elapsed after spraying ended) for NP1 and P2 respectively. The figure insets show the axisymmetric cross-section shape of the claddings and the positions from which stress, phase fraction and temperature is plotted: “interface” is a point 1.5 mm from the interface into the cladding and “surface” is a point 1 mm into the cladding from the top surface.

Immediately after spraying, the cladding surface and interface region temperatures were above the local martensite start temperature (refer to Table 2) and the cladding was comprised entirely of austenite ( $\gamma$ -Fe) with a CTE of  $18.7 \mu \text{K}^{-1}$  i.e. the cladding had a

CTE larger than the mild steel substrate ( $14.4 \mu \text{K}^{-1}$ ). The cladding surface region temperature was lower than the internal, interface region because the cold atomizer gas continued to flow over the cladding surface. As cooling progressed, martensite thus formed first at the cladding surface as it cooled below  $M_s$ , and then progressively throughout the cladding, progressively evolving a cladding tensile stress, balanced by a growing compressive stress in the substrate (not shown).

As the volume fraction of  $\alpha'$ -Fe (CTE  $= 11.6 \mu \text{K}^{-1}$ ) continued to increase in the cladding during further cooling towards room temperature, the local effective CTE decreased and at a mixture of 0.6 martensite and 0.4 austenite, the effective local CTE was approximately the same as the mild steel substrate. At higher fractions of martensite, the CTE became lower than that of the mild steel substrate. At this point there was, a turning point in the stress profiles in Fig. 10a and b as the previously evolved tensile stresses in the cladding started to be relieved by the comparatively fast shrinking of the predominantly martensitic cladding. After final cooling fully to room temperature, there was a small residual compressive stress at the interface but a much larger residual compressive stress at the cladding surface. These plots show that residual stresses cannot be easily estimated in advance for any particular spray forming condition because the local fractions of austenite and martensite – with significantly different CTEs changed continuously during cooling, the detail of which was dependent on the process parameters [36], supporting the need for these type of simulations over simplified analytical approaches. At room temperature, the martensite fraction in the surface region was  $\sim 0.95$  for both NP1 and P2 and 0.79 and 0.78 in the interface region respectively.

The comparison between the simulated and ND residual stress measurements showed that a relatively high mechanical integrity interfacial bonding could only be formed if there was sufficient substrate pre-heating before spraying. Clad tube P1 was pre-heated only to  $\sim 1020 \text{ K}$  and the cladding delaminated during post-spray cooling. Clad tube P2 was pre-heated to  $\sim 1270 \text{ K}$  and the resulting metallurgical bond was sufficient to maintain integrity at room temperature. Thus, the pre-heat temperature threshold sufficient for the interfacial bond development in the present case lies within the range of 70%–85% of the sprayed alloy solidus temperature of  $1495.5 \text{ K}$ .

The effects of different substrate pre-heat temperatures on the microstructure and thermal residual stresses developed were also simulated using clad tube P2 spraying parameters given in Table 1, but for different induction pre-heating voltages. Fig. 11a shows that the estimated cladding local CTE generally increased with substrate pre-heat temperature because of an increase in the  $\gamma$ -Fe fraction, which in turn changed the cladding local CTE, as described earlier. Although it may be generally expected that room temperature residual stresses will increase with substrate/cladding temperature, the simultaneous effect on the phase fractions and the resulting CTE variations can give counter-intuitive effects on substrate final residual stresses i.e. reduced final residual stresses with increasing pre-heat temperature, as shown in Fig. 11b.

Although the thermal residual stress gradient across the interface can be further reduced by increasing the  $\gamma$ -Fe fraction further, and bond mechanical integrity may be expected due to increased interfacial diffusion, at prolonged pre-heat temperatures much above  $1270 \text{ K}$ , it may also be expected that the mild steel tube substrate will lose its structural integrity, soften and distort during manufacture if excessive pre-heating were used.

As shown in Fig. 8, clad tube NP1 was manufactured using relatively high spray temperatures to provide a high heat flux essential to minimize the “cold” and porous transient regions in the first deposited layers of the cladding, and to promote interfacial

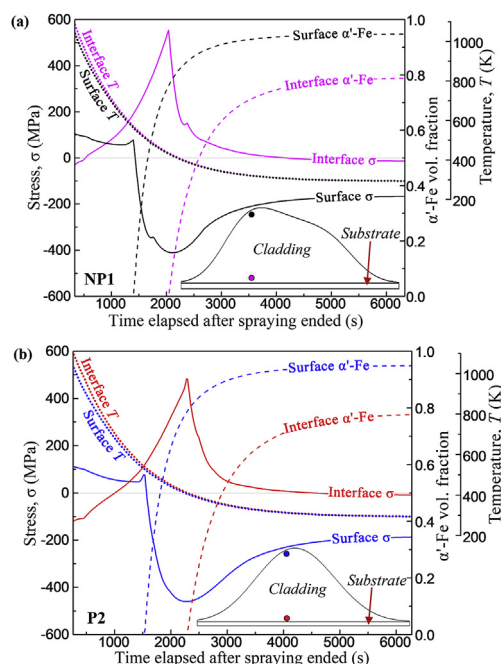
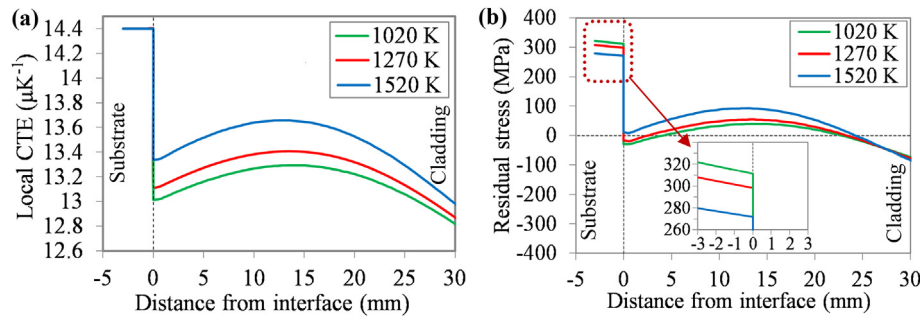
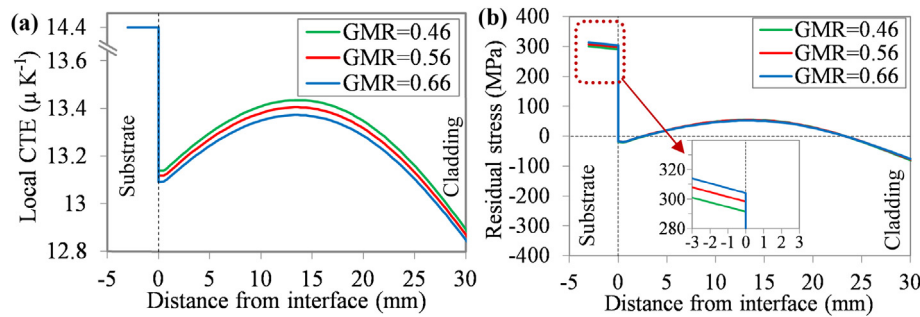


Fig. 10. Calculated hoop stress, martensite  $\alpha'$ -Fe volume fraction and temperature as a function of post-spray time in clad tubes (a) NP1 and (b) P2. The figure insets show the axisymmetric cross-section shape of the clad tubes and the corresponding positions (marked as points) at which the data is plotted.





**Fig. 11.** (a) The simulated local CTE distribution as a result of changes in the cladding local phase fraction due to different substrate pre-heat temperatures while maintaining the same spray forming temperature; (b) the corresponding simulated thermal residual hoop stress distribution in clad tube P2 at different substrate pre-heat temperatures, due to the induced changes in the relative local phase fractions and effective CTE.



**Fig. 12.** (a) The simulated local CTE distribution as a result of changes in the cladding local phase fraction due to different spray gas-to-melt flow ratios (GMR), where a high GMR reduces the spray temperature; (b) the corresponding simulated thermal residual hoop stress distribution in clad tube P2 at different GMR due to changes in the local CTE distribution.

diffusion. However, the build-up of an excessive liquid fraction in this case caused poor final cladding surface quality and the interfacial bonding was inconsistent along the interface. As described previously, this trade-off between low porosity and acceptable cladding surface quality was avoided in cladding P2 by spray forming at a relatively long spray distance to reduce alloy liquid fraction in the cladding during spraying and by pre-heating the substrate to compensate for the reduced incoming heat flux. Microstructural characterization (see Fig. 5) showed that pre-heating promoted micro-scale interfacial diffusion when spraying at longer spray distances (lower spray temperature). Overall, optimizing both pre-heat and spray temperatures is key to ensuring good interfacial bond formation. For example, the effects of changing the spray temperature on the thermal residual stress and microstructures developed can be simulated based on clad tube P2 spraying parameters but with different gas-to-melt flow ratios (GMR). Fig. 12a shows that a colder spray (higher GMR) leads to a larger CTE mismatch developed between the substrate and cladding due to the increased fraction of  $\alpha'$ -Fe in the cladding. Thus, a colder spray leads to a higher thermal residual stress mismatch across the interface, as shown in Fig. 12b, which may be detrimental to the interfacial bond integrity.

## 5. Conclusions

The mechanical integrity of bonding at the cladding-substrate interface of as-spray formed dissimilar steels clad tubes manufactured with different spray and substrate thermal conditions was assessed by comparing the thermal residual stress across the interface, simulated using a perfectly bonded cladding-substrate assumption, with measurements of residual stress obtained by neutron diffraction. Modelling and experimental data showed good

agreement, with increasing substrate pre-heat and spray temperatures advantageous in increasing cladding temperature that promoted interfacial diffusion, reduced porosity fraction and increased the fraction of retained austenite in the cladding that in turn reduced the coefficient of thermal expansion mismatch with the mild steel substrate. In the system studied here, the substrate pre-heat temperature threshold for interfacial bonding formation was within the range of 70%–85% of the spray formed alloy solidus temperature, which produced an interfacial shear strength that was ~90% of the shear strength of the mild steel substrate itself.

## Acknowledgements

The authors would like to acknowledge the funding from Baosteel Co. Ltd. Shanghai, China and the neutron beam time at ENGIN-X of ISIS Neutron Source, STFC Rutherford Appleton Laboratory, UK (Experiment No: RB1310425, RB1320313, RB1510231 and RB1810002). Dr. J. Fife from Paul Scherrer Institute is acknowledged for her support on the TOMCAT beamline, Swiss Light Source (Proposal No. 20141167 and 20150177). T.L. Lee gratefully acknowledges the University of Hull PhD Studentship awarded from 2011 to 2015. J. Mi also would like to acknowledge the financial support by the Royal Society Industry Fellowship awarded from 2012 to 2016.

## Appendix A. Supplementary data

Supplementary data related to this article can be found at <https://doi.org/10.1016/j.actamat.2018.05.055>.

## References

- [1] P.S. Grant, Spray forming, *Prog. Mater. Sci.* 39 (4–5) (1995) 497–545.
- [2] P.S. Grant, Solidification in spray forming, *Metall. Mater. Trans.* 38 (7) (2007) 1520–1529.
- [3] J. Mi, P.S. Grant, Modelling the shape and thermal dynamics of Ni superalloy rings during spray forming Part 1: shape modelling - droplet deposition, splashing and redeposition, *Acta Mater.* 56 (7) (2008) 1588–1596.
- [4] J. Mi, P.S. Grant, U. Fritsching, O. Belkessam, I. Garmendia, A. Landaberea, Multiphysics modelling of the spray forming process, *Mater. Sci. Eng., A* 477 (1) (2008) 2–8.
- [5] Y. Ikawa, T. Itami, K. Kumagai, Y. Kawashima, L. AG, B. RG, Spray deposition method and its application to the production of mill rolls, *ISIJ Int.* 30 (9) (1990) 756–763.
- [6] D. Hanlon, W. Rainforth, C. Sellars, R. Price, H. Gisborne, J. Forrest, The structure and properties of spray formed cold rolling mill work roll steels, *J. Mater. Sci.* 33 (13) (1998) 3233–3244.
- [7] J. Wahlroos, T. Liimatainen, Interface adherence of spray formed compound tube, in: J. Wood (Ed.), *Proceedings of the Second International Conference on Spray Forming*, Woodhead Pub., Swansea, U.K, 1993, pp. 225–234.
- [8] W. Cai, E. Lavernia, Modeling of porosity during spray forming, *Mater. Sci. Eng., A* 226 (1997) 8–12.
- [9] C. Meyer, N. Ellendt, L. Mädler, H.R. Müller, F. Reimer, V. Uhlenwinkel, Spray forming of high density sheets, *Mater. Werkst.* 45 (8) (2014) 642–651.
- [10] C. Cui, U. Fritsching, A. Schulz, Q. Li, Mathematical modeling of spray forming process of tubular preforms: Part 2, Heat transfer, *Acta Materialia* 53 (9) (2005) 2775–2784.
- [11] J. Mi, P.S. Grant, Modelling the shape and thermal dynamics of Ni superalloy rings during spray forming. Part 2: thermal modelling - heat flow and solidification, *Acta Mater.* 56 (7) (2008) 1597–1608.
- [12] P.S. Grant, B. Cantor, L. Katgerman, Modelling of droplet dynamic and thermal histories during spray forming—II. Effect of process parameters, *Acta Metall. Mater.* 41 (11) (1993) 3109–3118.
- [13] P.S. Grant, B. Cantor, Modelling of droplet dynamic and thermal histories during spray forming—III. Analysis of spray solid fraction, *Acta Metall. Mater.* 43 (3) (1995) 913–921.
- [14] T.L. Lee, J. Mi, S.L. Zhao, J.F. Fan, S.Y. Zhang, S. Kabra, P.S. Grant, Characterization of the residual stresses in spray-formed steels using neutron diffraction, *Scripta Mater.* 100 (0) (2015) 82–85.
- [15] R. McGrann, D. Greving, J. Shadley, E. Rybicki, T. Kruecke, B. Bodger, The effect of coating residual stress on the fatigue life of thermal spray-coated steel and aluminum, *Surf. Coating. Technol.* 108 (1998) 59–64.
- [16] J.R. Santisteban, M.R. Daymond, J.A. James, L. Edwards, ENGIN-X: a third-generation neutron strain scanner, *J. Appl. Crystallogr.* 39 (6) (2006) 812–825.
- [17] D.S. Kupperman, S. Majumdar, J.P. Singh, A. Saigal, Application of neutron diffraction time-of-flight measurements to the study of strain in composites, in: M. Hutchings, A. Krawitz (Eds.), *Measurement of Residual and Applied Stress Using Neutron Diffraction*, Springer, Netherlands, 1992, pp. 439–450.
- [18] S. Ho, E.J. Lavernia, Thermal residual stresses in spray atomized and deposited Ni3Al, *Scripta Mater.* 34 (4) (1996) 527–536.
- [19] Available from: <<http://www.matweb.com/search/datasheet.aspx?matguid=f936a4bfa744495c9185774f811c6e28>> [accessed on 11.11.2016].
- [20] Available from: <<http://www.matweb.com/search/datasheet.aspx?matguid=7ab1936975fd4cb2937286a8a004e052>> [accessed on 12.11.2016].
- [21] Available from: <<http://www.matweb.com/search/DataSheet.aspx?MatGUID=a2eed65d6e5e4b66b7315a1b30f4b391>> [accessed on 13.11.2016].
- [22] J. Chen, B. Young, B. Uy, Behavior of high strength structural steel at elevated temperatures, *J. Struct. Eng.* 132 (12) (2006) 1948–1954.
- [23] N. Chawla, X. Deng, Microstructure and mechanical behavior of porous sintered steels, *Mater. Sci. Eng.* 390 (1–2) (2005) 98–112.
- [24] N. Ramakrishnan, V.S. Arunachalam, Effective elastic moduli of porous ceramic materials, *J. Am. Ceram. Soc.* 76 (11) (1993) 2745–2752.
- [25] R. Hardin, C. Beckermann, Effect of porosity on deformation, damage, and fracture of cast steel, *Metall. Mater. Trans.* 44 (12) (2013) 5316–5332.
- [26] P. Withers, M. Johnson, J. Wright, Neutron strain scanning using a radially collimated diffracted beam, *Phys. B Condens. Matter* 292 (3) (2000) 273–285.
- [27] P. Withers, H. Bhadeshia, Residual stress. Part 1—measurement techniques, *Mater. Sci. Technol.* 17 (4) (2001) 355–365.
- [28] H. Rietveld, A profile refinement method for nuclear and magnetic structures, *J. Appl. Crystallogr.* 2 (2) (1969) 65–71.
- [29] A.C. Larson, R.B.V. Dreele, General Structure Analysis System (GSAS), Los Alamos National Laboratory Report LAUR 86-748, 2004.
- [30] R.J. Hill, C.J. Howard, Quantitative phase analysis from neutron powder diffraction data using the Rietveld method, *J. Appl. Crystallogr.* 20 (6) (1987) 467–474.
- [31] G.A. Roberts, R. Kennedy, G. Krauss, Tool Steels, fifth ed., ASM International, 1998.
- [32] D. Koistinen, R. Marburger, A general equation prescribing the extent of the austenite-martensite transformation in pure iron-carbon alloys and plain carbon steels, *Acta Metallurgica* 7 (1) (1959) 59–60.
- [33] H.G. Nanesa, M. Jahazi, R. Naraghi, Martensitic transformation in AISI D2 tool steel during continuous cooling to 173 K, *J. Mater. Sci.* (2015) 1–11.
- [34] BS EN 15340:2007, Thermal spraying — determination of shear load resistance of thermally sprayed coatings, British Standards Institution, 2007, pp. 1–18.
- [35] C.A. Andersen, M.F. Hasler, Extension of electron microprobe techniques to biochemistry by the use of long wavelength X-rays, in: R. Castaing, P. Deschamps, J. Philibert (Eds.), *Proceedings of the Fourth International Conference on X-ray Optics and Microanalysis*, 1966, pp. 310–327. Hermann, Paris.
- [36] R. Ristau, A. Becker, V. Uhlenwinkel, R. Kienzler, Simulations of temperatures, residual stresses, and porosity measurements in spray formed super alloys tubes, in: *Superalloy 718 and Derivatives*, John Wiley & Sons, Inc, 2010, pp. 470–485.